Showcasing research from the team of Prof. Hahn and Dr Breitung at the Institute of Nanotechnology, Karlsruhe Institute of Technology, Baden-Württemberg, Germany.

Multi-anionic and -cationic compounds: new high entropy materials for advanced Li-ion batteries

Multi-anionic and -cationic high entropy compounds have been used for the first time as cathodes for Li-ion batteries, facilitating new concepts for future Li-based energy storage technologies. The versatility in composition and the high configurational entropy of the compounds allow for the tailoring of electrochemical properties such as increased capacity retention, and the decrease of toxic materials (*e.g.* Co, Ni). Cover artwork by Christian Grupe.

As featured in:

See Qingsong Wang, Horst Hahn, Ben Breitung *et al.*, *Energy Environ. Sci.*, 2019, **12**, 2433.

ROYAL SOCIETY OF CHEMISTRY | Celebrating IYPT 2019

rsc.li/ees

PAPER

Multi-anionic and -cationic compounds: new high entropy materials for advanced Li-ion batteries†

Qingsong Wang, [ID] *[a] Abhishek Sarkar, [ID] [ab] Di Wang, [ac] Leonardo Velasco, [ID] [a] Raheleh Azmi, [ID] [d] Subramshu S. Bhattacharya, [e] Thomas Bergfeldt, [c] Andre Düvel, [ID] [f] Paul Heitjans, [ID] [f] Torsten Brezesinski, [ID] [a] Horst Hahn [ID] *[abg] and Ben Breitung [ID] *[ac]

In the present work, a new class of high entropy materials for energy storage applications is introduced. Multi-anionic and -cationic compounds are prepared by facile mechanochemistry using a recently designed multi-cationic transition-metal-based high entropy oxide as the precursor and LiF or NaCl as the reactant, leading to formation of lithiated or sodiated materials. Notably, the Li-containing entropy-stabilized oxyfluoride described herein ($Li_x(Co_{0.2}Cu_{0.2}Mg_{0.2}Ni_{0.2}Zn_{0.2})OF_x$) exhibits a working potential of 3.4 V *vs.* Li^+/Li, enabling its use as a cathode active material. Unlike conventional (non-entropy-stabilized) oxyfluorides, this new material shows enhanced Li storage properties due to entropy stabilization, which, in general, facilitates tailoring the cycling performance by varying the constituent elements in yet unprecedented ways. In addition, we demonstrate that the concept of entropy stabilization is also applicable to Na-containing oxychlorides with a rock-salt structure, thus paving the way toward development of (next-generation) post-Li battery technologies.

Broader context

The continuous pursuit of new and advanced materials to enable next-generation applications is a grand challenge facing materials science. In the electrochemical energy storage field, lithium-ion batteries are being considered indispensable for large-scale applications such as in hybrid and full-electric vehicles. Cathode active materials are crucial for further improving the energy density to allow for longer driving ranges of battery-powered vehicles. Herein, a new class of high entropy materials is introduced, with the anion and cation lattices contributing to the configurational entropy. Specifically, Li-containing high entropy oxyfluoride, exhibiting a working potential of 3.4 V *vs.* Li^+/Li, shows enhanced lithium storage properties due to entropy stabilization. Notably, mechanochemical synthesis enabled the incorporation of not only lithium but also sodium, thus paving the way toward rational design of post-lithium battery technologies. Taken together, multi-anionic and multi-cationic high entropy compounds represent a potentially transformative materials class with unprecedented properties.

[a] *Institute of Nanotechnology, Karlsruhe Institute of Technology (KIT), Hermann-von-Helmholtz-Platz 1, 76344 Eggenstein-Leopoldshafen, Germany. E-mail: qingsong.wang@kit.edu, horst.hahn@kit.edu, ben.breitung@kit.edu*

[b] *Joint Research Laboratory Nanomaterials – Technische Universität Darmstadt and Karlsruhe Institute of Technology (KIT), Otto-Berndt-Str. 3, 64206 Darmstadt, Germany*

[c] *Karlsruhe Nano Micro Facility (KNMF), Karlsruhe Institute of Technology (KIT), Hermann-von-Helmholtz-Platz 1, 76344 Eggenstein-Leopoldshafen, Germany*

[d] *Institute for Applied Materials, Karlsruhe Institute of Technology (KIT), Hermann-von-Helmholtz-Platz 1, 76344 Eggenstein-Leopoldshafen, Germany*

[e] *Department of Metallurgical and Materials Engineering, Nano Functional Materials Technology Centre (NFMTC), Indian Institute of Technology Madras, Chennai, 600036, India*
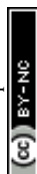
[f] *Institute of Physical Chemistry and Electrochemistry, and ZFM – Center for Solid State Chemistry and New Materials, Leibniz University Hannover, Callinstr. 3a, 30167 Hannover, Germany*

[g] *Helmholtz Institute Ulm for Electrochemical Energy Storage, Helmholtzstr. 11, 89081 Ulm, Germany*

† Electronic supplementary information (ESI) available. See DOI: 10.1039/c9ee00368a

Introduction

High entropy materials (HEMs) are gaining significant interest due to their novel and often unexpected and unprecedented properties in many different areas of application.[1–4] HEMs are based on the premise of introducing a high configurational entropy (S_{config}) to stabilize a single-phase structure. A prominent and already well-established group of HEMs are the metallic high entropy alloys (HEAs).[5–9] Recently, the same concept was applied to ionic compounds where multiple cations occupy the same lattice, thus increasing S_{config}.[1,10–12] A large number of such high entropy compounds have been synthesized and reported, including carbides,[11,13] diborides,[2] nitrides,[14,15] chalcogenides[12,16] and oxides,[1,17–19] with wide-ranging applications as thermoelectrics,[12,16] dielectrics[19] and for lithium-ion

This journal is © The Royal Society of Chemistry 2019

Energy Environ. Sci., 2019, **12**, 2433–2442 | 2433

batteries.[20,21] The latter HEMs, named high entropy oxides (HEOs), have been reported only since 2015 by the pioneering work of Rost *et al.*[1]

However, until now, there are no literature reports on HEM compounds with more than one anion. Hence, the stabilizing S_{config} effect only results from the cations present in the crystal structure (eqn (S1), ESI†), since the contribution from the anion site is zero. For this reason, the preparation of a multi-anionic and multi-cationic single-phase structure, showing clear indications of entropy stabilization, is of great interest, especially considering that the configurational entropy gain would be even larger compared to the transition-metal-based HEO systems.

Herein, we report, to the best of our knowledge for the first time, on multi-anionic and multi-cationic high entropy oxyhalides with application in electrochemical energy storage. A multi-cationic transition-metal-based HEO (*i.e.*, only oxygen ions occupy the anion site) was used as the precursor and additional halide (X) and alkali metal ions were introduced to produce a multi-anionic and multi-cationic rock-salt type compound (HEOX). The introduction of monovalent fluorine into the anion lattice of HEO, occupied by divalent oxygen, is charge compensated by incorporation of monovalent lithium (or sodium) into the cation lattice. Since fluorine and oxygen have similar ionic radii (1.33 Å *vs.* 1.40 Å, respectively),[22] such substitution can be achieved without inducing significant strain in the single-phase rock-salt structure. Despite their chemical complexity, the preparation of HEOXs is simple and easily scalable, using a facile mechanochemical (ball-milling) process with HEO and LiF or NaCl as the precursor and reactant, respectively. Specifically, $Li_x(Co_{0.2}Cu_{0.2}Mg_{0.2}Ni_{0.2}Zn_{0.2})OF_x$ and $Na_y(Co_{0.2}Cu_{0.2}Mg_{0.2}Ni_{0.2}Zn_{0.2})OCl_y$, referred to as Li(HEO)F and Na(HEO)Cl in the following, were synthesized and characterized, with special emphasis placed on the Li(HEO)F compound.

Considering the crystal field concept, metal fluorides, in general, possess higher electrochemical potential than oxides due to the strongly ionic character of M–F bonds.[23,24] This is also why metal oxides and fluorides have been explored as potential anode and cathode active materials, respectively, in the past.[25–29] Here, the incorporation of fluorine increased the working potential to 3.4 V *vs.* Li+/Li, compared to around 1.0 V for the respective transition-metal-based HEOs,[20,21,30,31] thus rendering Li(HEO)F interesting for application as a (next-generation) positive electrode material. The overall redox mechanism appears to be similar to that observed for Li-rich disordered rock-salt oxides, as indicated by X-ray diffraction, transmission electron microscopy and X-ray photoelectron spectroscopy.[32]

Results and discussion

Materials characterization

The most commonly known HEOs are transition-metal-based rock-salt oxides such as $(Co_{0.2}Cu_{0.2}Mg_{0.2}Ni_{0.2}Zn_{0.2})O$.[1,20,33,34] Very recently, HEOs were utilized as anode active materials in

Li-ion cells, showing high specific capacity while maintaining good capacity retention.[20,21] It is assumed that this materials system undergoes a conversion reaction within an entropy-stabilized matrix, facilitating the re-integration of redox-active ions into the lattice during delithiation. Based on the work on HEOs, both Li(HEO)F and Na(HEO)Cl were synthesized by means of high-energy ball-milling. Because none of the late 3d transition metals (Mn, Co, Ni, Cu, Zn) has been reported to form oxyfluorides through soft chemistry or solid-state reaction routes,[35,36] ball-milling appears to be the most efficient way to prepare such solid solution phases.[37–39]

Fig. 1a shows X-ray diffraction (XRD) patterns obtained on the as-prepared Li(HEO)F and a mixture of pristine HEO and LiF. The latter compounds exhibit a rock-salt structure with lattice parameter $a_{HEO} = 4.233$ Å and $a_{LiF} = 4.035$ Å (from Rietveld analysis, Fig. S1, ESI†). After 24 h of ball-milling a 1:1 molar mixture of HEO and LiF, single-phase Li(HEO)F was obtained. The diffraction pattern can still be indexed to a cubic rock-salt phase, but with a lattice parameter $a = 4.185$ Å, clearly lying between that of pristine HEO and LiF. For the Rietveld refinement, the instrumental parameters were taken into account using reference data obtained on LaB_6 (NIST 660a). The microstructural parameters (crystallite size and micro-strain) were adequately refined to adjust the peak shapes. Thermal displacement parameters were constrained to be the same for all of the atoms to minimize quantification errors. As shown in the inset of Fig. 1 and in Table S1 (ESI†), the Li and F atoms are randomly distributed on the respective cation and anion sub-lattices of the rock-salt HEO. The substitution of transition-metal cations by Li is evident from the decrease in intensity of the (111) reflection. This is due to the lower atomic number of Li compared to the other transition metals. For O and F, the atomic numbers and ionic radii are similar, and in a rock-salt lattice, there is typically only one site (4b) where the F− ions can reside. Overall, XRD indicates that the LiF is successfully incorporated into the HEO structure.

In order to confirm the presence of lithium and fluorine in the lattice structure, solid-state magic angle spinning (MAS) nuclear magnetic resonance (NMR) spectroscopy measurements were conducted on the as-prepared material. Fig. 1b shows the 7Li- and 19F-MAS-NMR spectra of both Li(HEO)F and a physical mixture of HEO and LiF (see ref. 40–42 for reviews of 7Li- and 19F-NMR on energy-related materials). The incorporation of Li+ and F− into the HEO leads to a different chemical environment compared to the LiF reference material. Because the local elemental distribution in Li(HEO)F is random, the number of chemical environments is rather large, therefore, line broadening occurs. In addition, the paramagnetic Co^{2+} causes a strong line broadening. The narrow lines at −38 ppm and −1.05 ppm in the 19F- and 7Li-MAS-NMR spectrum, respectively, can be assigned to unreacted LiF. Curve fitting revealed the presence of around 8% LiF (Fig. S2, ESI†). Because LiF was neither detected by selected-area electron diffraction (SAED) nor by XRD, it seems reasonable to assume that the ball-milling process left behind some amorphous material, as also reported for Li_2VO_2F compounds.[37] High-resolution X-ray photoelectron

2434 | *Energy Environ. Sci.*, 2019, **12**, 2433–2442

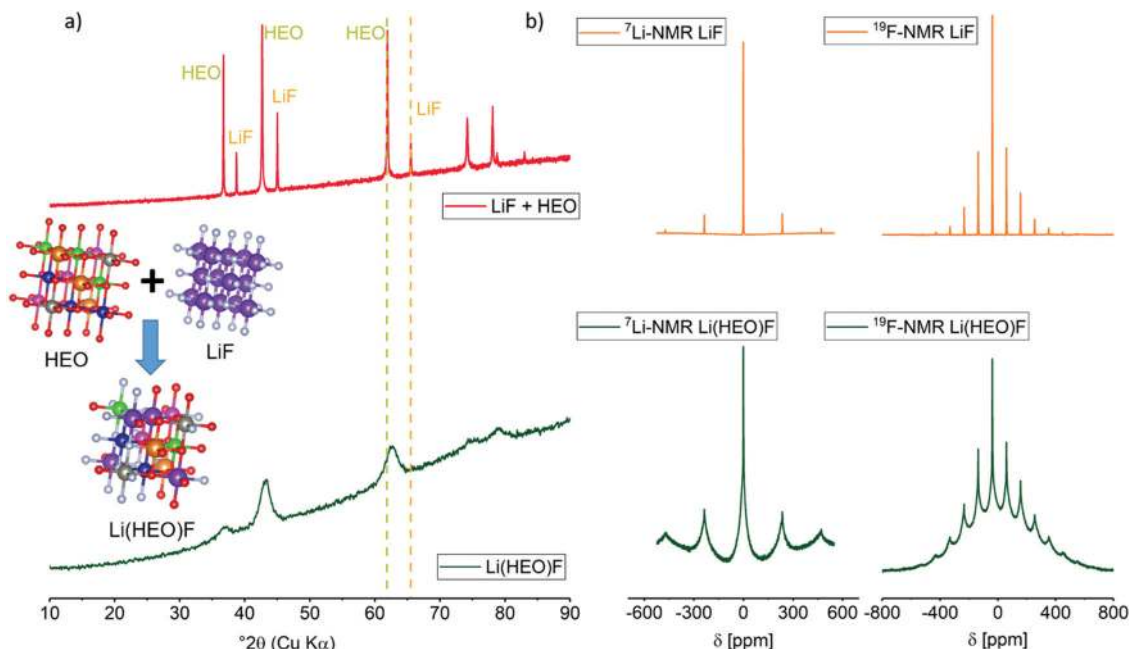This journal is © The Royal Society of Chemistry 2019

Fig. 1 (a) XRD pattern obtained on both a physical mixture of LiF and HEO and the as-prepared Li(HEO)F. Dashed lines denote the position of the (220) reflection of LiF and HEO. For Li(HEO)F, the (220) reflection is located between that of LiF and HEO, indicating successful incorporation of Li^+ and F^- into the HEO lattice. Oxygen is in red, fluorine in white, nickel in pink, cobalt in blue, magnesium in orange, copper in green, zinc in grey and lithium in violet in the cubic structures shown in the inset. (b) ^7Li- and ^{19}F-MAS-NMR of LiF and the as-prepared Li(HEO)F (recorded with ν_{rot} = 55 kHz, $\nu_0(^7Li)$ = 233.3 MHz, $\nu_0(^{19}F)$ = 564.8 MHz). Distinct line broadening is observed in the Li(HEO)F case due to changes in chemical environment.

spectroscopy (XPS) measurements were conducted on a powder sample to gain further insights into the oxidation state(s) of the respective elements. The F 1s peaks (Fig. S3, ESI†) at 685.2 eV and 686.5 eV seem to indicate the successful incorporation of fluorine into the HEO structure, since these binding energies can be referred to MOF, MF and MOF_2 binding motifs.[43,44] The Li 1s spectrum reveals two peaks at binding energies of 55.2 eV and 56.1 eV, indicating two different Li^+ chemical environments, namely, oxygen and fluorine. The Co species are identified as being mainly Co^{2+} (91% Co^{2+}/9% Co^{3+}), while Ni exists as mixture of Ni^{2+} (37% of total Ni ions) and Ni^{3+} (63% of total Ni ions).[45,46] The Cu 2p spectrum is found to only exhibit a single peak at 933 eV. The lack of a satellite peak hints at either Cu^{1+} or Cu^0. However, a clear distinction using the Cu LMM Auger peak was not possible, since it overlaps with that of the Zn LMM.[47] Nevertheless, Cu^{1+} is assumed to be present in the Li(HEO)F compound. The peak at 1303.8 eV in the Mg 1s spectrum can be attributed to Mg^{2+},[48,49] and the Zn $2p_{3/2}$ at 1021.3 eV and Zn LMM at 988.6 eV are indicative of Zn^{2+}.[50–52]
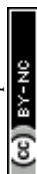
'NaCl' has also been successfully added to the HEO structure through an identical ball-milling approach. Because the ionic radius of Cl^- is much larger than that of O^{2-} or F^-, and Na^+ is larger than Li^+ (Cl^- = 1.81 Å, O^{2-} = 1.40 Å, F^- = 1.33 Å, Na^+ = 1.02 Å, Li^+ = 0.76 Å),[22] it is more difficult to achieve an entropy-stabilized single-phase structure. The incorporation of a reasonable fraction of different size ions (Na^+, Cl^-) would lead to a major distortion of the lattice, destabilizing the structure. Hence, in the NaCl case, the maximum fraction that can be added to the entropy-stabilized HEO material is expected to be

much lower than for LiF. According to XRD (Fig. 2), the Na(HEO)Cl compound also exhibits a single-phase rock-salt structure with the characteristic reflections shifted toward smaller Bragg angles as compared to pristine HEO (12:1 molar ratio of HEO and NaCl, $a_{Na(HEO)Cl}$ = 4.244 Å, a_{NaCl} = 5.642 Å, see Fig. S1, ESI†).

The concept of entropy stabilization was evaluated for Li(HEO)F in the present work. Because a single-phase entropy-stabilized structure segregates into multiple phases at low temperature ($T\Delta S$ is small), but will re-form a single phase at high temperature ($T\Delta S$ is large), as shown previously,[1,53] this behavior can be used to corroborate the entropy stabilization effect. To this end, the XRD pattern obtained on single-phase Li(HEO)F heated to 750 °C was analyzed in some more detail (Fig. S1, ESI†). As it is evident from the splitting of reflections (apparently, LiF and different metal oxide phases form), phase segregation indeed occurs. This provides clear evidence that entropy plays a major role in stabilizing the chemically complex system $Li_x(Co_{0.2}Cu_{0.2}Mg_{0.2}Ni_{0.2}Zn_{0.2})O_xF_x$.

Fig. 3 shows results from high-resolution transmission electron microscopy (HRTEM) and SAED on the Li(HEO)F. The aggregates have an average size of 100 nm (Fig. 3a), with good crystallinity (Fig. 3b) of the rock-salt structure, while SAED indicates that the as-prepared material is obtained without other (crystalline) secondary phases.

The lattice parameter of the rock-salt structure was calculated from both the SAED and HRTEM data and agrees well with the Rietveld refinement result (Fig. S1, ESI†). The homogeneous distribution of elements, as mentioned above, was
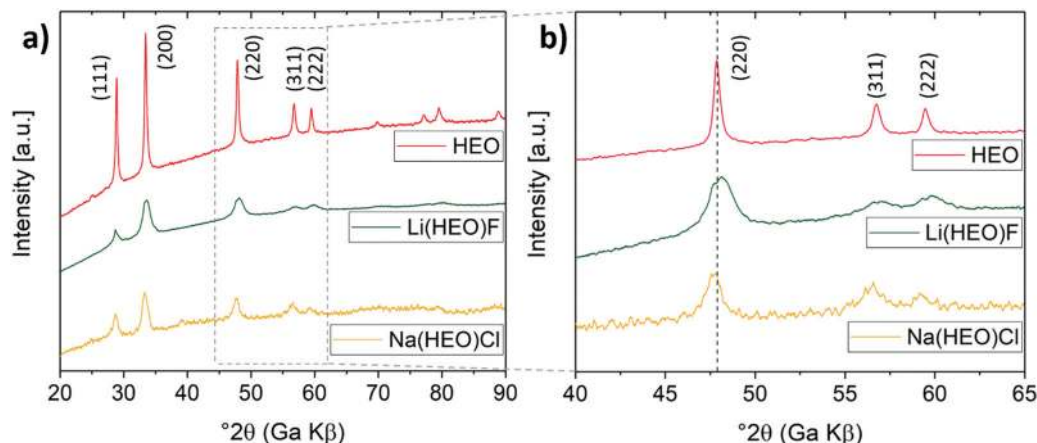
This journal is © The Royal Society of Chemistry 2019

Energy Environ. Sci., 2019, 12, 2433–2442 | 2435

Fig. 2 (a) XRD patterns of HEO, Li(HEO)F and Na(HEO)Cl. The shift in reflection position toward smaller and larger Bragg angles for Na(HEO)Cl and Li(HEO)F, respectively, relative to pristine HEO, is denoted by a dashed line in (b).
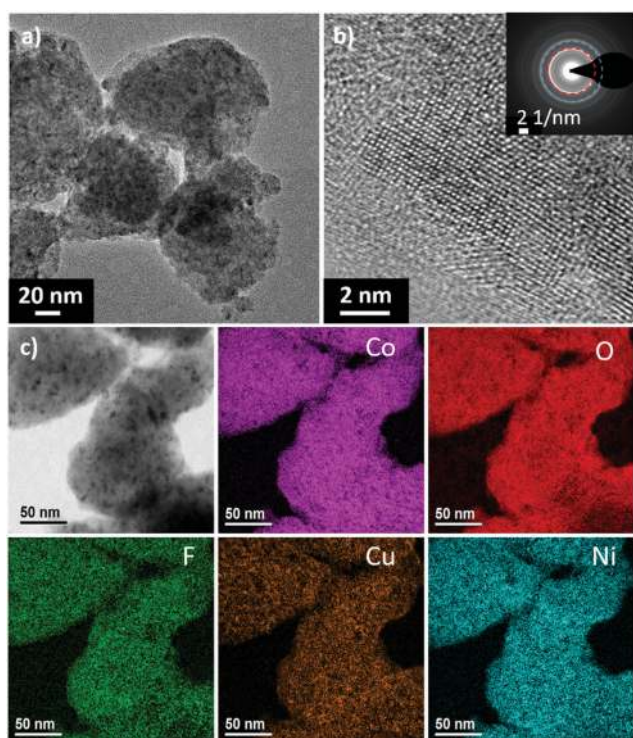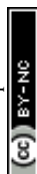

Fig. 3 (a and b) TEM images at different magnification of the as-prepared Li(HEO)F showing crystalline particles around 100 nm in size. The inset in (b) is an SAED pattern obtained on the same material. The (200) and (220) reflections are denoted by red and blue circles, respectively. (c) EFTEM mapping results revealing uniform element distribution.

confirmed by energy-filtered TEM (EFTEM) mapping (Fig. 3c). Of note, both Mg and Zn are not depicted because of the lack of sufficient signal intensity for the corresponding core-loss edges. Nevertheless, the uniform distribution of each single element in the Li(HEO)F was also corroborated by spectrum imaging using energy dispersive X-ray (EDX) spectroscopy in scanning TEM (STEM) mode (Fig. S4, ESI†). Within the resolution of the two methods (both approaching the sub-nanometer

level), there is no notable elemental segregation or clustering, both of which would lead to a decrease in the number of possible microstates, and therefore, lower the configurational entropy. Finally, inductively-coupled plasma optical emission spectroscopy (ICP-OES) measurements were conducted on the Li(HEO)F to examine the chemical composition. The combined results from ICP-OES, NMR and EDX reveal an overall composition of $Li_{0.94}(Co_{0.21}Ni_{0.21}Zn_{0.2}Mg_{0.2}Cu_{0.18})O_1F_{0.87}$, as shown and discussed in Fig. S5 (ESI†).

Electrochemical characterization

The introduction of the multi-anionic concept enabled the use of the high entropy oxyfluoride as a new cathode active material for rechargeable Li-ion cells. Notably, the incorporation of fluorine into the structure increased the working potential significantly. In the present work, we show, to the best of our knowledge for the first time, the utilization of an entropy-stabilized compound as a cathode active material for reversible energy storage. The benefits arising from the high entropy crystal structure with respect to the electrochemical performance comprise the capacity retention and Li-extraction ability of the compound. In general, oxyfluorides represent an important class of electrode materials, owing to their ability to suppress oxygen loss during cycling operation. The latter is often observed for state-of-the-art cathode materials and can lead to capacity degradation.[32,54–57] The incorporated fluorine renders the material resistant against HF etching. Note that HF is usually formed in the electrolyte due to reaction of trace water (or protic species) with $LiPF_6/PF_5$.[58] Therefore, oxyfluoride-based electrode materials have been the subject of intense investigations in recent years.[59–61] With our approach, we aim at combining the advantages of oxyfluorides with the benefits arising from the entropy stabilization. However, the objective of this study was not to optimize the cycling performance, but rather to demonstrate the applicability of high entropy cathode active materials in the forefront field of electrochemical energy storage. Optimization regarding choice of binder, electrolyte, material preparation, additives etc. needs

2436 | Energy Environ. Sci., 2019, **12**, 2433–2442

This journal is © The Royal Society of Chemistry 2019

to be done in the next step. Here, the electrochemical properties of Li(HEO)F are compared with rock-salt type LiNiOF, which was prepared in the same way. Because LiNiOF shows a much lower S_{config} than Li(HEO)F, but also contains Ni as the redox active cation, it is an ideal reference compound to evaluate the entropy stabilization concept for Li-insertion materials.

Electrochemical testing of the as-prepared Li(HEO)F and pure HEO was performed on half-cells with a Li metal counter electrode. For HEO, cyclic voltammetry (CV) shows the already reported cathodic peak around 0.5 V in the initial cycle and around 0.8 V in the subsequent cycles, characteristic of the anode conversion reaction upon lithiation (Fig. 4a).[20] In contrast, for Li(HEO)F, a cathodic peak around 3.4 V is observed from the CV curves (Fig. 4b), which is in agreement with the galvanostatic discharge profiles shown in Fig. 4c. Regarding energy density, a middle discharge potential of 3.4 V is superior to most disordered rock-salt oxyfluoride materials reported in the literature, showing potentials closer to 2.5 V.[36,37,62,63] The higher working potential compared to pure HEO is due in part to the fact that the overall (de)lithiation mechanism changed from a conversion to an insertion type reaction.
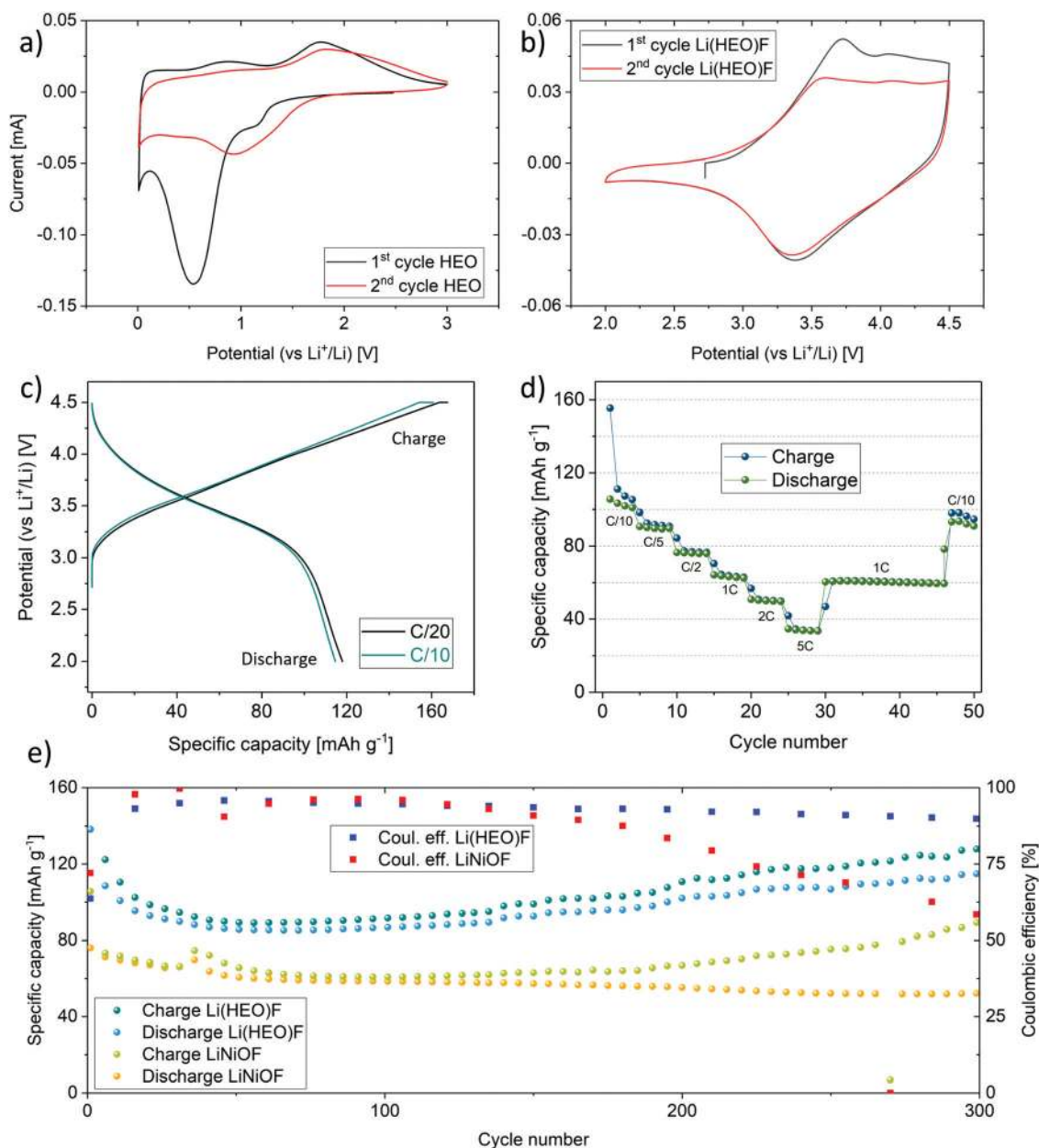

Fig. 4 Cyclic voltammetric curves at a sweep rate of 0.1 mV s^{-1} for (a) pure HEO cycled in the voltage range between 0.01 and 3.0 V vs. Li$^+$/Li and (b) Li(HEO)F between 2.5 and 4.5 V vs. Li$^+$/Li. (c) Charge/discharge curves for Li(HEO)F-based half-cells at rates of C/20 (10 mA g^{-1}) and C/10 (20 mA g^{-1}). The cut-off potentials were set at 2.0 and 4.5 V vs. Li$^+$/Li. (d) Specific capacities as a function of cycle number for rates ranging from C/10 to 5C. (e) Comparison of the capacity retention at C/10 of Li(HEO)F and LiNiOF.
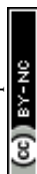
More importantly, the incorporation of fluorine leads to an increase in the Gibbs free energy of the system, and therefore, to a higher theoretical potential of the redox reaction (see discussion in the ESI†).[64] Note that the application of Li(HEO)F in rechargeable Li-ion batteries is also fostered by its relatively high lithium content. Overall, this entropy-stabilized oxyfluoride compound fulfills one of the most important requirements of a cathode active material for graphite-based cells—it is capable of serving as the lithium source.

As shown in Fig. 4c, specific capacities of 168 and 161 mA h g^{-1} were achieved in the initial charge cycle (with a constant voltage step at 4.5 V) at C/20 and C/10, respectively. The specific discharge capacity was around 120 mA h g^{-1} at both rates. The initial capacity loss is due in part to electrolyte degradation and formation of a solid electrolyte interphase (SEI) layer.[36] During the course of cycling, the specific capacity, especially at low C-rates, decreases slightly, as can be seen from the rate performance data in Fig. 4d. However, other side reactions associated with the cathode active material cannot be ruled out, accounting for the difference in the charge and discharge capacities at low C-rates. It should be noted that the cell chemistry has not been optimized yet. Nevertheless, the specific capacity at C/10 can be recovered virtually completely after applying high rates of up to 5C.

A direct comparison of the cyclability at C/10 of Li(HEO)F to LiNiOF is presented in Fig. 4e. From the data shown, it is evident that the Li(HEO)F delivers higher specific capacities than LiNiOF. This is noteworthy because the redox-active nickel has been replaced by other elements; both cobalt and nickel are likely the only species to be oxidized during delithiation. The molar fraction of Co and Ni together amounts to only 0.4 instead of 1 for LiNiOF. This means that despite the decrease in redox-active ion fraction, the specific capacity is increased.

After around 150 cycles, the Coulombic efficiency clearly shows differences between the entropy-stabilized Li(HEO)F and the non-entropy stabilized LiNiOF. While the Coulombic efficiency tends to decrease rapidly for the LiNiOF system, in the Li(HEO)F, it remains fairly stable. The entropy stabilization seems to play a key role in maintaining high reversible capacities and stabilizing the Coulombic efficiency. In general, oxide and/or oxyfluoride cathode active materials show some oxygen (anion) redox activity at high potential, leading to oxygen evolution at the particle/electrolyte interface, and therefore, formation of an oxygen deficient material.[32,56,59] Note that oxygen release adversely affects the cycling stability of any electrode material. In a nutshell, the entropy stabilization of the Li(HEO)F compound is capable of somewhat counteracting this kind of degradation. Nevertheless, in this regard, it is important to note that the Coulombic efficiencies for both materials are lower compared to state-of-the-art cathode active materials.

A higher reversible capacity directly relates to the capability of the material in providing access to mobile Li in the structure. Most commonly, not all of the Li in the lattice is accessible, since it is contributing to some degree to the structural stability. Using the entropy stabilization approach, it seems

that more Li can be extracted, thus leading to the observed increase in specific capacity compared to LiNiOF. The theoretical specific capacities of Li(HEO)F and LiNiOF are similar with 278 and 266 mA h g^{-1}, respectively, when assuming a one-electron redox process per formula unit. However, because only 0.8 Li$^+$ can presumably be extracted from the Li(HEO)F, the theoretical specific capacity drops to 222 mA h g^{-1}. This can be explained as follows: Cu^{2+} (after the initial cycle; see section on redox mechanism below), Mg^{2+} and Zn^{2+} in the Li(HEO)F structure cannot be oxidized, and therefore, Ni^{2+} and Co^{2+} are the only remaining redox-reactive cations in the potential range applied (based on the assumption that the divalent state of the cations is prevailing). Finally, we note that improvements in cycling performance, especially the specific capacity, can be expected when even more lithium is incorporated into the rock-salt lattice, as shown recently for Li-rich disordered rock-salt materials.[65,66]

Reaction mechanism

XRD and TEM experiments were conducted on the Li(HEO)F at different states of charge (SOC) during cycling to gain more insight into the reaction mechanism (Fig. 5a). The parent rock-salt structure was preserved throughout cycling and no secondary (crystalline) phases were detected. As can be seen in Fig. 5a, the reflections in the *ex situ* XRD pattern clearly shift toward larger Bragg angles (smaller lattice parameter) in the charge cycle, thus hinting at an insertion mechanism.[32] Li extraction from the Li(HEO)F is accompanied by transition-metal oxidation (presumably Ni^{2+} and/or Co^{2+}), leading to a decrease in ionic radius, and therefore, to a smaller unit cell. Yet, the reflections shift back to their original position upon subsequent lithiation, emphasizing the reversibility of the Li insertion/extraction process. These findings are also supported by SAED. The patterns shown in Fig. 5a confirm the preservation of the rock-salt lattice upon cycling.

The changes in oxidation state of the elements upon cycling were examined by *ex situ* XPS. The corresponding measurements were performed on electrodes with different states of charge/discharge (equivalent to *ex situ* XRD in Fig. 5a). The Li 1s, F 1s and Co 2p spectra in Fig. 5b emphasize the reversibility of the Li extraction/insertion during charge/discharge. Note that utilizing a multiplet splitting approach for quantified oxidation state analysis of Co ions was hampered by the low concentration of active material at the top surface of the electrode, leading to the presence of very low intensity peaks. Qualitative analysis reveals that in the pristine electrode, the Co ions are predominantly present as Co^{2+}. This is due to the existence of a strong satellite peak about 6 eV higher in binding energy than the main peak, which can be considered characteristic of Co^{2+}.[46] This satellite peak disappears after delithiation, thus indicating oxidation of Co^{2+} to Co^{3+}. After lithiation, the re-appearance of a less intense satellite peak suggests co-existence of Co^{3+} and Co^{2+} ions.[46,47,51,52] In the F 1s spectra, the peak at 685.2 eV can be assigned to the fluorine ions in the Li(HEO)F rock-salt structure, as discussed above (Fig. S3, ESI†). This peak slightly shifts to lower binding energy (684.4 eV) after
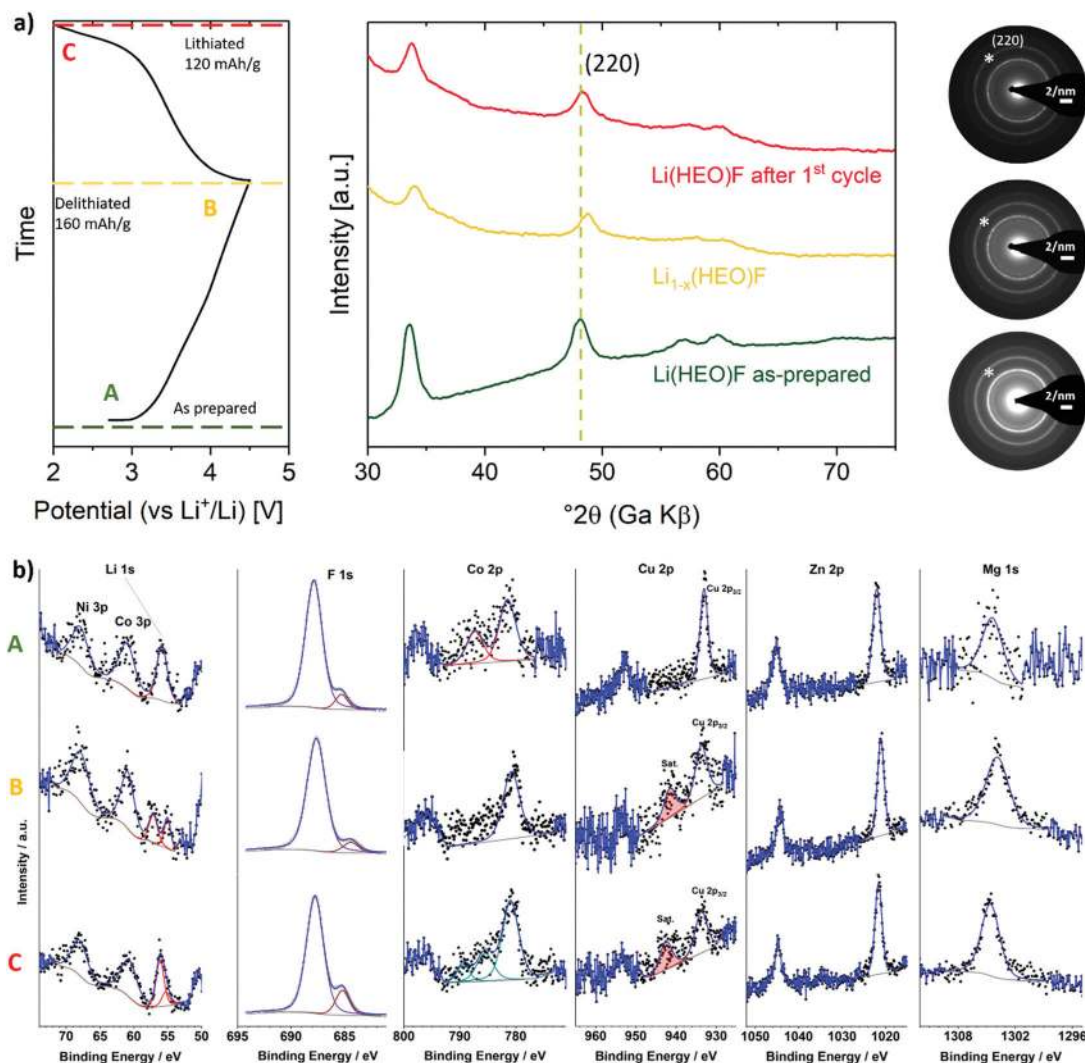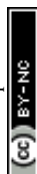
2438 | *Energy Environ. Sci.*, 2019, **12**, 2433–2442

This journal is © The Royal Society of Chemistry 2019

Fig. 5 (a) Initial charge/discharge curve at C/10 (20 mA g^{-1}) in the voltage range between 2.0 and 4.5 V (left) and the corresponding *ex situ* XRD patterns collected under an Ar atmosphere using a protective Kapton film (middle) as well as SAED data (right). The (220) reflection is denoted by an asterisk in the SAED patterns. (b) XPS spectra of the Li 1s, F 1s, Co 2p, Cu 2p, Zn 2p and Mg 1s core levels − before and after cycling (A: pristine state, B: after delithiation and C: after re-lithiation).

delithiation, probably because of a lower electron density around the fluorine atoms after Li extraction. As expected, it shifts back to 685.2 eV with re-lithiation. The major peak located at around 687.9 eV in the F 1s spectra is due to the polyvinylidene difluoride (PVdF) binder used, which remains unaltered during cycling.[67] In the Cu 2p spectra, the appearance of a satellite peak ($\sim$942 eV) after delithiation and subsequently re-lithiation is indicative of the oxidation of Cu^{1+} to Cu^{2+}.[47] Such (surface) oxidation, which apparently is not reversible, seems to contribute to some extent to the irreversible capacity loss in the initial cycle (Fig. 4c). As expected, both Mg and Zn remain in divalent state during cycling, thus providing evidence that they are indeed redox-inactive. Unfortunately, the analysis of Ni oxidation state was hampered by superposition of the Ni 2p and F KLL peaks (Fig. S6, ESI†). The XPS results were also confirmed by electron energy loss spectroscopy (EELS, data not shown). In addition,

EELS indicated that the bulk Cu in the as-prepared material has a mixed oxidation state of Cu^{1+}/Cu^{2+}.

Conclusions

With the incorporation of multiple anions into an entropy-stabilized multi-cationic compound, we were able to show, for the first time, that not only the cations but also the anions can be varied while preserving a single-phase rock-salt structure. These compounds constitute a new class of entropy-stabilized materials, with the anion lattice also contributing to the configurational entropy, resulting in an additional structural stabilization gain. Using this approach, we successfully synthesized an oxyfluoride cathode active material with a rock-salt structure for next-generation Li-ion battery applications. Notably, the entropy stabilization improved the cycling performance

This journal is © The Royal Society of Chemistry 2019

Energy Environ. Sci., 2019, **12**, 2433–2442 | **2439**

considerably. Additionally, this approach enables the reduction of toxic and costly elements in battery cathodes, without significantly affecting the energy density. Taken together, the concept of multi-anionic and multi-cationic high entropy compounds introduces a new class of energy storage materials with unprecedented properties.

Methods

Synthesis

HEO was prepared by a reverse co-precipitation process, followed by high-temperature calcination, the details of which can be found elsewhere.[53] For the synthesis of Li(HEO)F, a 1:1 molar ratio of LiF (Alfa Aesar, 99.99%) and HEO was ball-milled using a high-energy planetary ball-mill (Retsch PM 100, Retsch GmbH). Na(HEO)Cl was prepared in the same way but with a 12:1 molar ratio of HEO and NaCl (Alfa Aesar, >99%). Specifically, WC vials (50 ml in volume) and WC balls (4 mm in diameter) were used, with a 40:1 ball-to-powder weight ratio. The milling process was carried out at 500 rpm for 24 h in an Ar atmosphere. The as-prepared powder was collected and stored inside an Ar-filled glovebox.

Electrochemistry

For the cathode preparation, active material (100 mg), Super C65 carbon black (28.6 mg, Timcal) and polyvinylidene difluoride (14.3 mg, Solef 5130) were uniformly dispersed into N-methyl-2-pyrrolidone. The resulting slurry was doctor-bladed onto an Al current collector and dried in a vacuum oven at 80 °C for 12 h. Circular electrodes (13 mm in diameter) were cut from the cathode sheet, assembled in an Ar-filled glovebox and tested in CR2032 coin cells. 1 M LiPF$_6$ in a 3:7 weight mixture of ethylene carbonate/ethyl methyl carbonate (Selectilyte LP57, BASF SE), glass microfiber filter paper (GF/C, Whatman™) and Li metal foil (Gelon LIB Co., Ltd) were used as the electrolyte, separator and counter electrode, respectively. Galvanostatic cycling measurements were performed on an Arbin battery test system (BT-2000) at room temperature. Cyclic voltammetry was performed on a Bio-logic potentiostat (VMP3). The areal cathode active material loading was about 1 mg cm^{-2}. The specific capacity was calculated based on the total weight of cathode active material in the electrode.

Characterization

XRD patterns for the as-prepared compounds were recorded using a STOE Stadi P diffractometer with Cu-Kα radiation. The powder was filled into borosilicate glass capillaries (Hilgenberg) with inner diameter of 0.48 mm and wall thickness of 0.01 mm. For the cycled samples, the powder was collected from the electrode inside an Ar-filled glovebox and measured under inert conditions using a STOE Stadi P diffractometer, equipped with a Ga-jet X-ray source (Ga-Kβ radiation).

ICP-OES spectroscopy (iCAP 7600 ICP-OES DUO, Thermo Fisher Scientific) was conducted on 5 to 6 mg samples

(±0.05 mg accuracy) dissolved into hydrochloric and nitric acid. More details can be found in the ESI.†

TEM measurements were conducted on powder samples dispersed on a holey carbon-coated gold grid. The samples were loaded onto a Gatan vacuum-transfer holder inside an Ar-filled glovebox and transferred to the TEM without exposure to air. TEM, SAED, EFTEM and STEM-EDX/EELS data were collected using a FEI Titan 80-300 microscope, equipped with a CEOS image spherical aberration corrector, a HAADF STEM detector (Fischione model 3000), EDAX SUTW EDX detector and a Tridiem Gatan image filter. The microscope was operated at an accelerating voltage of 300 kV.

^{7}Li- and ^{19}F-NMR data were acquired at room temperature on a Bruker Avance III 600 spectrometer (14 T) at Larmor frequencies of 233.3 and 564.8 MHz, respectively. A 1.3 mm high-speed probe was used for magic-angle spinning experiments. The samples were spun at 55 kHz. For the ^{19}F-MAS-NMR measurements, a Hahn-Echo experiment was performed (pi/2 pulse: 1 μs), while the ^{7}Li-MAS-NMR spectra were recorded with a single-pulse experiment (pi/2 pulse: 1.1 μs). As reference substances for the chemical shifts, both a dilute solution of LiCl and liquid C$_6$F$_6$ were used.

XPS measurements on the as-prepared powder and cycled samples at different states of charge were performed directly on the powder and recovered electrode tape using a K-Alpha+ instrument (Thermo Fisher Scientific) with a monochromatic Al-Kα X-ray source (1486.6 eV) with 400 μm spot size. The K-Alpha+ charge compensation system was applied to prevent localized charge buildup during analysis, using 8 eV electrons and low-energy Ar ions. Data acquisition and processing were carried out using the software Thermo Avantage.[68] The spectra were fitted with one or more Voigt profiles. The binding energies are reported with respect to the binding energy of C 1s for hydrocarbon at 285.0 eV. The analyzer transmission function, Scofield sensitivity factors[69] and effective attenuation lengths (EALs) for photoelectrons were applied for quantification. EALs were calculated using the standard TPP-2M formalism.[70]

Data availability

The data used for this study are available from the corresponding authors upon request.

Author contributions

2440 | *Energy Environ. Sci.*, 2019, **12**, 2433–2442

This journal is © The Royal Society of Chemistry 2019

electrochemical characterization. Q. W., H. H. and B. B. supervised the synthesis and experiments, directed the project and co-wrote the manuscript. All the authors contributed to the data analysis, discussion and manuscript preparation.

Conflicts of interest

The authors declare no competing financial interest.

Acknowledgements

References

1 C. M. Rost, E. Sachet, T. Borman, A. Moballegh, E. C. Dickey, D. Hou, J. L. Jones, S. Curtarolo and J.-P. Maria, *Nat. Commun.*, 2015, **6**, 8485.

2 J. Gild, Y. Zhang, T. Harrington, S. Jiang, T. Hu, M. C. Quinn, W. M. Mellor, N. Zhou, K. Vecchio and J. Luo, *Sci. Rep.*, 2016, **6**, 37946.

3 D. B. Miracle and O. N. Senkov, *Acta Mater.*, 2017, **122**, 448–511.

4 J. W. Yeh and S. J. Lin, *J. Mater. Res.*, 2018, **33**, 3129–3137.

5 J.-W. Yeh, S.-K. Chen, S.-J. Lin, J.-Y. Gan, T.-S. Chin, T.-T. Shun, C.-H. Tsau and S.-Y. Chang, *Adv. Eng. Mater.*, 2004, **6**, 299–303.

6 Y. J. Zhou, Y. Zhang, Y. L. Wang and G. L. Chen, *Appl. Phys. Lett.*, 2007, **90**, 181904.

7 M.-H. Tsai, C.-W. Wang, C.-W. Tsai, W.-J. Shen, J.-W. Yeh, J.-Y. Gan and W.-W. Wu, *J. Electrochem. Soc.*, 2011, **158**, H1161.

8 W.-Y. Tang, M.-H. Chuang, H.-Y. Chen and J.-W. Yeh, *Surf. Coat. Technol.*, 2010, **204**, 3118–3124.

9 F. Tian, L. K. Varga, N. Chen, J. Shen and L. Vitos, *Intermetallics*, 2015, **58**, 1–6.

10 W. J. Shen, M. H. Tsai, K. Y. Tsai, C. C. Juan, C. W. Tsai, J. W. Yeh and Y. S. Chang, *J. Electrochem. Soc.*, 2013, **160**, C531–C535.

11 E. Castle, T. Csanádi, S. Grasso, J. Dusza and M. Reece, *Sci. Rep.*, 2018, **8**, 8609.

12 R. Z. Zhang, F. Gucci, H. Zhu, K. Chen and M. J. Reece, *Inorg. Chem.*, 2018, **57**, 13027–13033.

13 J. Zhou, J. Zhang, F. Zhang, B. Niu, L. Lei and W. Wang, *Ceram. Int.*, 2018, **44**, 22014–22018.

14 C.-W. Tsai, S.-W. Lai, K.-H. Cheng, M.-H. Tsai, A. Davison, C.-H. Tsau and J.-W. Yeh, *Thin Solid Films*, 2012, **520**, 2613–2618.

15 T. Jin, X. Sang, R. R. Unocic, R. T. Kinch, X. Liu, J. Hu, H. Liu and S. Dai, *Adv. Mater.*, 2018, **30**, 1707512.

16 R. Liu, H. Chen, K. Zhao, Y. Qin, B. Jiang, T. Zhang, G. Sha, X. Shi, C. Uher, W. Zhang and L. Chen, *Adv. Mater.*, 2017, **29**, 1–7.

17 A. Sarkar, R. Djenadic, D. Wang, C. Hein, R. Kautenburger, O. Clemens and H. Hahn, *J. Eur. Ceram. Soc.*, 2018, **38**, 2318–2327.

18 J. Dąbrowa, M. Stygar, A. Mikuła, A. Knapik, K. Mroczka, W. Tejchman, M. Danielewski and M. Martin, *Mater. Lett.*, 2018, **216**, 32–36.

19 D. Bérardan, S. Franger, D. Dragoe, A. K. Meena and N. Dragoe, *Phys. Status Solidi RRL*, 2016, **10**, 328–333.

20 A. Sarkar, L. Velasco, D. Wang, Q. Wang, G. Talasila, L. de Biasi, C. Kübel, T. Brezesinski, S. S. Bhattacharya, H. Hahn and B. Breitung, *Nat. Commun.*, 2018, **9**, 3400.

21 H. Chen, N. Qiu, S. Sun, Y. Wang, Y. Cui and Z. Yang, *J. Alloys Compd.*, 2018, **777**, 767–774.

22 R. D. Shannon, *Acta Crystallogr., Sect. A: Cryst. Phys., Diffr., Theor. Gen. Crystallogr.*, 1976, **32**, 751–767.

23 J. B. Goodenough, *Advances in Lithium-Ion Batteries*, Springer US, Boston, MA, 2002, pp. 135–154.

24 G. G. Amatucci and N. Pereira, *J. Fluorine Chem.*, 2007, **128**, 243–262.

25 X. L. Huang, X. Zhao, Z. L. Wang, L. M. Wang and X. B. Zhang, *J. Mater. Chem.*, 2012, **22**, 3764–3769.

26 Y. Huang, X. L. Huang, J. S. Lian, D. Xu, L. M. Wang and X. B. Zhang, *J. Mater. Chem.*, 2012, **22**, 2844–2847.

27 X. L. Huang, R. Z. Wang, D. Xu, Z. L. Wang, H. G. Wang, J. J. Xu, Z. Wu, Q. C. Liu, Y. Zhang and X. B. Zhang, *Adv. Funct. Mater.*, 2013, **23**, 4345–4353.

28 D. L. Ma, Z. Y. Cao, H. G. Wang, X. L. Huang, L. M. Wang and X. B. Zhang, *Energy Environ. Sci.*, 2012, **5**, 8538–8542.

29 P. K. Nayak, L. Yang, W. Brehm and P. Adelhelm, *Angew. Chem., Int. Ed.*, 2018, **57**, 102–120.

30 Q. Wang, A. Sarkar, Z. Li, Y. Lu, L. Velasco, S. S. Bhattacharya, T. Brezesinski, H. Hahn and B. Breitung, *Electrochem. Commun.*, 2019, **100**, 121–125.

31 A. Sarkar, Q. Wang, A. Schiele, M. R. Chellali, S. S. Bhattacharya, D. Wang, T. Brezesinski, H. Hahn, L. Velasco and B. Breitung, *Adv. Mater.*, 2019, 1806236.

32 R. A. House, L. Jin, U. Maitra, K. Tsuruta, J. W. Somerville, D. P. Förstermann, F. Massel, L. Duda, M. R. Roberts and P. G. Bruce, *Energy Environ. Sci.*, 2018, **11**, 926–932.

33 D. Bérardan, S. Franger, A. K. Meena and N. Dragoe, *J. Mater. Chem. A*, 2016, **4**, 9536–9541.

34 H. Chen, J. Fu, P. Zhang, H. Peng, C. W. Abney, K. Jie, X. Liu, M. Chi and S. Dai, *J. Mater. Chem. A*, 2018, **6**, 11129–11133.

35 B. L. Chamberland, A. W. Sleight and W. H. Cloud, *J. Solid State Chem.*, 1970, **2**, 49–54.

36 L. Zhang, D. Dambournet, A. Iadecola, D. Batuk, O. J. Borkiewicz, K. M. Wiaderek, E. Salager, M. Shao, G. Chen and J. M. Tarascon, *Chem. Mater.*, 2018, **30**, 5362–5372.
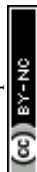
37 R. Chen, S. Ren, M. Knapp, D. Wang, R. Witter, M. Fichtner and H. Hahn, *Adv. Energy Mater.*, 2015, **5**, 1401814.

38 Y. Tomita, H. Nasu, Y. Izumi, J. Arai, S. Otsuka, Y. Yamane, K. Yamada, Y. Kohno and K. Kobayashi, *J. Power Sources*, 2016, **329**, 406–411.

39 Y. Tomita, N. Kimura, H. Nasu, Y. Izumi, J. Arai, Y. Yamane, K. Yamada, Y. Kohno and K. Kobayashi, *J. Appl. Electrochem.*, 2017, **47**, 1057–1063.

40 C. P. Grey and N. Dupré, *Chem. Rev.*, 2004, **104**, 4493–4512.

41 C. V. Chandran and P. Heitjans, *Annu. Rep. NMR Spectrosc.*, 2016, **89**, 1–102.

42 M. Wilkening, A. Düvel, F. Preishuber-Pflügl, K. Da Silva, S. Breuer, V. Šepelák and P. Heitjans, *Z. Kristallogr. – Cryst. Mater.*, 2017, **232**, 107–127.

43 Y. T. Sul, *Int. J. Nanomed.*, 2010, **5**, 87–100.

44 K. I. Murai, Y. Suzuki, T. Moriga and A. Yoshiasa, *AIP Conf. Proc.*, 2007, **882**, 463–465.

45 A. W. Moses, H. G. G. Flores, J. G. Kim and M. A. Langell, *Appl. Surf. Sci.*, 2007, **253**, 4782–4791.

46 R. Azmi, V. Trouillet, M. Strafela, S. Ulrich, H. Ehrenberg and M. Bruns, *Surf. Interface Anal.*, 2018, **50**, 43–51.

47 M. C. Biesinger, L. W. M. Lau, A. R. Gerson and R. S. C. Smart, *Appl. Surf. Sci.*, 2010, **257**, 887–898.

48 J. Y. Zhang, G. Yang, S. G. Wang, Y. W. Liu, Z. D. Zhao, Z. L. Wu, S. L. Zhang, X. Chen, C. Feng and G. H. Yu, *J. Appl. Phys.*, 2014, **116**, 1–6.

49 M. Morales, *Int. J. Green Technol.*, 2018, **3**, 51–62.

50 Z. Zhao, G. Tian, A. Sarapulova, V. Trouillet, Q. Fu, U. Geckle, H. Ehrenberg and S. Dsoke, *J. Mater. Chem. A*, 2018, **6**, 19381–19392.

51 V. Kumar, C. R. Mariappan, R. Azmi, D. Moock, S. Indris, M. Bruns, H. Ehrenberg and G. Vijaya Prakash, *ACS Omega*, 2017, **2**, 6003–6013.

52 C. R. Mariappan, V. Kumar, R. Azmi, L. Esmezjan, S. Indris, M. Bruns and H. Ehrenberg, *CrystEngComm*, 2018, **20**, 2159–2168.

53 A. Sarkar, R. Djenadic, N. J. Usharani, K. P. Sanghvi, V. S. K. Chakravadhanula, A. S. Gandhi, H. Hahn and S. S. Bhattacharya, *J. Eur. Ceram. Soc.*, 2017, **37**, 747–754.

54 B. Xu, C. R. Fell, M. Chi and Y. S. Meng, *Energy Environ. Sci.*, 2011, **4**, 2223–2233.

55 T. Bartsch, F. Strauss, T. Hatsukade, A. Schiele, A.-Y. Kim, P. Hartmann, J. Janek and T. Brezesinski, *ACS Energy Lett.*, 2018, **3**, 2539–2543.

56 T. Hatsukade, A. Schiele, P. Hartmann, T. Brezesinski and J. Janek, *ACS Appl. Mater. Interfaces*, 2018, **10**, 38892–38899.

57 L. de Biasi, A. Schiele, M. Roca-Ayats, G. Garcia, T. Brezesinski, P. Hartmann and J. Janek, *ChemSusChem*, 2019, DOI: 10.1002/cssc.201900032.

58 C. L. Campion, W. Li and B. L. Lucht, *J. Electrochem. Soc.*, 2005, **152**, A2327–A2334.

59 S. K. Jung, H. Gwon, J. Hong, K. Y. Park, D. H. Seo, H. Kim, J. Hyun, W. Yang and K. Kang, *Adv. Energy Mater.*, 2014, **4**, 1–7.

60 L. Li, B. H. Song, Y. L. Chang, H. Xia, J. R. Yang, K. S. Lee and L. Lu, *J. Power Sources*, 2015, **283**, 162–170.

61 Z. Lun, B. Ouyang, D. A. Kitchaev, R. J. Clément, J. K. Papp, M. Balasubramanian, Y. Tian, T. Lei, T. Shi, B. D. McCloskey, J. Lee and G. Ceder, *Adv. Energy Mater.*, 2019, **9**, 1802959.

62 S. W. Kim, N. Pereira, N. A. Chernova, F. Omenya, P. Gao, M. S. Whittingham, G. G. Amatucci, D. Su and F. Wang, *ACS Nano*, 2015, **9**, 10076–10084.

63 R. Chen, E. Maawad, M. Knapp, S. Ren, P. Beran, R. Witter and R. Hempelmann, *RSC Adv.*, 2016, **6**, 65112–65118.

64 M. S. Islam and C. A. J. Fisher, *Chem. Soc. Rev.*, 2014, **43**, 185–204.

65 A. Urban, J. Lee and G. Ceder, *Adv. Energy Mater.*, 2014, **4**, 1400478.

66 J. Lee, D. A. Kitchaev, D. H. Kwon, C. W. Lee, J. K. Papp, Y. S. Liu, Z. Lun, R. J. Clément, T. Shi, B. D. McCloskey, J. Guo, M. Balasubramanian and G. Ceder, *Nature*, 2018, **556**, 185–190.

67 T. Zhang, Y. He, F. Wang, H. Li, C. Duan and C. Wu, *Sep. Purif. Technol.*, 2014, **138**, 21–27.

68 K. L. Parry, A. G. Shard, R. D. Short, R. G. White, J. D. Whittle and A. Wright, *Surf. Interface Anal.*, 2006, **38**, 1497–1504.

69 J. H. Scofield, *J. Electron Spectrosc. Relat. Phenom.*, 1976, **8**, 129–137.

70 S. Tanuma, C. J. Powell and D. R. Penn, *Surf. Interface Anal.*, 2011, **43**, 689–713.

2442 | *Energy Environ. Sci.*, 2019, **12**, 2433–2442

This journal is © The Royal Society of Chemistry 2019